LA-UR-03-760

Title: PENETRATION OF HLSA-100 STEEL WITH TUNGSTEN CARBIDE SPHERES AT STRIKING VELOCITIES BETWEEN 0.8 AND 2.5 KM/SEC

Author(s): Rick L. Martineau (X-2)
Michael B. Prime (ESA-WR)
Thomas Duffey

Los Alamos

NATIONAL LABORATORY

Penetration of HSLA-100 Steel with Tungsten Carbide Spheres at Striking Velocities Between 0.8 and 2.5 km/sec

Rick L. Martineau[a,*], Michael B. Prime[b], and Thomas Duffey[c]

[a] Group X-2, MS T085, Los Alamos National Laboratory, Los Alamos, NM, 87545, USA

[b] Group ESA-WR, MS P946, Los Alamos National Laboratory, Los Alamos, NM, 87545, USA

[c] Consulting Engineer, P.O. Box 1239, Tijeras, NM 87059, USA

Abstract

A 51 mm thick plate of High-Strength Low-Alloy (HSLA-100) steel was impacted by 6.4 mm diameter tungsten carbide spheres traveling at velocities ranging from 0.8-2.5 km/sec. The width and depth of the crater for each impact event are provided in tabulated form and graphed as a function of velocity. The impacts were simulated using an explicit Lagrangian finite element model. A residual stress map over a cross-section through the crater was also measured by the Contour Method for the 2.2 km/sec impact. The predominant feature of the stress map was a peak compressive stress of 1100 MPa, which is 1.6 times the yield strength, centered approximately one crater diameter below the crater floor. Residual stresses in the as-received HSLA-100 plate were also measured and were used to evaluate the effect of initial stresses on the model prediction. Good agreement is shown between the numerical simulation of the impact event and the experimental data.

Background

The effect of impact and penetration on the subsequent performance of components and structures is receiving increased attention, most notably in studies of foreign object damage (FOD). The term "foreign object damage" originated to describe damage on the blades in jet aircraft turbine engines. Such damage is caused by impingement of debris, sand, hailstones, etc. High-cycle fatigue, the leading cause of failure for these engines, usually occurs in the impacted region [1]. These regions are later affected by factors such as residual stress, stress concentrations, microstructural damage, and cracks formed as a result of the impact. Recent studies have isolated the residual stress effects and have shown that they play a major role in the observed degradation of fatigue life [2,3,4,5]. The drastic effect of a high velocity impact on the fatigue crack propagation rate has been further examined in the recent experimental work by Lanciotti [6], who studied the result of space debris impact on simulated space structures.

Only a few experimental measurements of the residual stresses resulting from an impact or penetration have been reported in the literature, such as a fairly simple test to estimate the surface residual stresses after an impact event on an aluminum plate [6]. Recently, synchrotron X-ray diffraction [7,8] was used to examine residual strains in the region of a dynamic impact onto a plate of Ti-6Al-4V [4,9]. Although these two studies are the most extensive measurements to date of damaged induced residual stresses, the work by Peter et al. [4] was performed at much lower impact velocities than in this study, and the work by Boyce et al. [9] only measured the surface stresses, due to experimental limitations.

Several recent studies have been performed involving the impact of tungsten carbide spheres on a variety of different target materials and thicknesses, and over a wide range in impact velocities. Grady [10] reports experiments on using tungsten carbide solid spheres to impact thin plastic and glass target materials at impact velocities in the range 2-4 km/sec. The solid spheres underwent failure and dynamic fragmentation, with incipient failure at the lowest velocities, and extremely intense particulation at the highest impact velocities. The sphere impact data are complemented by both dynamic compression (Hugoniot elastic limit and shock EOS) and dynamic tension (spall) test data for tungsten carbide. Williams [11] investigates the role of phase changes on impact parameters using a tungsten carbide sphere impacting a lead target. Impact velocities were in the range 2.7-8.3 km/sec, somewhat higher than those considered by Grady [10], and crater parameters were reported. It was found that both crater depth and crater diameter are linear functions of impact velocity, i.e., the influence of phase changes is not reflected in these parameters. Wang, et al. [12] investigate numerically and experimentally the low-speed (0.02-0.3 km/sec) impact behavior of a tungsten carbide sphere into semi-infinite white cast iron targets. It appears the projectiles were effectively rigid at this impact velocity level. Crater depth increased monotonically with impact velocity. Finite Element simulations of plastic deformation and lip formation were in excellent agreement with experimental measurements of crater diameter, depth and lip height. FE predictions included predicting the stress state in the target developed during impact.

Other recent work reported for sphere impact involves materials other than tungsten carbide. Peters et al. [4] examined the effects of 1 and 3.2 mm diameter chrome-hardened

steel spheres on the fatigue life of Ti-6Al-4V. Fatigue cracks and high tensile residual stresses were observed from the 0.2-0.3 km/sec impacts. Tanabe, et al. [13] report the impact of a ferrite sphere into four types of semi-infinite carbon targets in the impact velocity range of 0.6-1.5 km/sec. It was found in this experimental study that crater depth is mainly controlled by the impact pressure (i.e., impact velocity) and the fracturing of the projectile. Impacts of copper spheres into relatively thin hardened steel plates are reported by Grady and Kipp [14] in a study of the mechanisms of breakup and disintegration of sphere and target. The role of phase-change phenomena on sphere impact is reported by Hertel, et al. [15].

Considerable recent work has been reported on hypervelocity impact of spheres as well. For example, Orphal [16] investigates penetrating projectile fragments for highly oblique impact of stainless steel spheres on thin laminated targets. Piekutowski [17] characterizes the sphere failure from plastic deformation through fracture and fragmentation up to complete disintegration of the sphere at higher impact velocities. A crater depth study for hypervelocity impact of a spherical projectile into a semi-infinite target is reported by Hayhurst, et al. [18].

No studies appear to have been performed on high velocity impact of HSLA steels, nor have any measurements of the residual stress state been performed on the targets following an impact above 0.3 km/sec. It is therefore the purpose of this paper to present results on the impact of tungsten carbide spheres on semi-infinite HSLA steel targets in the high-velocity range of 0.8-2.5 km/sec. HSLA alloys are of interest because of their high yield strength, toughness, and weldability, making them excellent candidates for the hulls on naval ships and blast loaded structures.

A second emphasis of the paper is to examine numerically and experimentally the residual stress state in the target material as a result of the impact and subsequent crater. The residual stresses are examined because of their possible effect on the ability of armor or turbine blades to survive multiple impacts or to survive future service loads when the original impact event did not cause total failure. In this paper, the Contour Method by Prime [19] was used to generate an experimentally measured map of sub-surface residual stresses from the impact of the spherical ball. Finite element models were used to predict both the geometry of the crater and the resulting residual stresses. Good comparisons are shown between the measured data and numerical predictions.

Experiments

The plate material used in this study (see Figure 1) is a low carbon, copper precipitation hardened, High-Strength Low-Alloy. This steel is often used for naval ship hulls, armor, and containment structures. The chemical composition of HSLA-100 is given in Table 1. The 51 mm thick plate material was prepared by hot cross-rolling. It was Austenized at 900 ºC for 75 minutes and then water quenched. The plate was then tempered at 660 ºC for 200 minutes followed by another water quench. A flame cut section of plate measuring 148 mm wide and 457 mm long was used for the impact experiments described in this study.

Tungsten carbide spheres were purchased from Machining Technologies, Inc. in Elmore, Ohio. The 6.35 mm diameter spheres were composed of 94% tungsten carbide with 6% of a cobalt binder. The spheres were Grade 25, Class C-2 material, where the grade

refers to a roundness tolerance of 0.000025 of an inch and Class C-2 refers to material with a hardness of 92 on the Rockwell A scale.

The steel plate was impacted normal to the plate surface by the small diameter spheres with velocities ranging from 0.8-2.5 km/sec. The projectiles were fired from a 12.7-mm (0.50-inch) smooth bore powder gun after being placed in a polyethylene obturator that was specifically designed to release the projectile during flight. A pair of light screens, which was placed between the gun and target, was used to measure the velocity of the projectile. An angled stripper plate was located between the light screens and target to further separate the projectile from the obturator. The impact events were spaced a minimum of one plate thickness (51 mm) from each other along the 457 mm length of the target plate, as shown in Figure 1, and both of the large 457 × 148 mm surfaces were used for experiments. The target centers on each side were off-set, thus minimizing the potential for the stress state associated with the craters on the back surface to influence the depth of penetration on the front surface. The impact velocity, depth, width, and crater volume of the resulting crater are shown in Table 2. The depth and width of the crater, which were measured relative the planar surface of the plate, are plotted as a function of impact velocity in Figure 2. It is interesting to note that the crater diameter is relatively linear with velocity, while the depth of penetration appears to roll over at approximately 1.5 km/sec.

A qualitatively similar rollover of the penetration depth vs. velocity curve has been reported elsewhere by Forrestal and Piekutowski [20] for the somewhat related situation involving spherical-nose steel projectiles, although their partitioning of the response into three regions as striking velocities increased is only partially valid for the brittle spherical

6

projectiles impacted in the present study. Hohler and Stilp [21] also present numerous

examples of this rollover, including for the closely related case of a projectile with length-to-

diameter ratio of 1.

The impacted region from the 2.2 km/sec experiment was later examined for residual

stresses. The resulting crater, which is shown in Figure 3, is approximately 10 mm in

diameter and 12 mm deep from the top of the lip to the bottom of the crater. The lip for the

2.2 km/sec crater is approximately 3.6 mm above the original planar surface.

Residual Stresses Measurements

The Contour Method [19] maps residual stresses using two experimental steps

followed by an analytical step. First, the material is carefully cut in two at the point of

interest. The cut surface deforms as residual stresses are released. Assuming the cut was

made on a flat plane, the deformed shape, or contour, is then uniquely related to the original

residual stresses. The second experimental step then measures the deformed shape, or

contour, of the cut surface. Assuming that stresses relaxed elastically because of the cut,

Bueckner's Superposition Principle [22] says that the original residual stresses normal to the

cut plane are given analytically by the pressures required to force the deformed surface back

to a flat plane [19]. In practice, the same answer is given more conveniently by starting with

a flat surface in a finite element (FE) model and deforming the surface into the opposite of

the measured contour. Since the displacements are small, the same result is returned. The

ability of the contour method to accurately measure a complex stress state has been

experimentally validated by comparison with a known stress specimen [19] and by

comparison with neutron diffraction measurements on a welded plate [23]. Because of space limitations in this paper, the reader is referred to other work [19] for details on the subtleties, assumptions, and limitations of the contour method.

In this study on the penetrated plate, the cut to measure residual stress was made with a Mitsubishi FX-10 wire Electric Discharge Machine (EDM) and a 150 μm diameter brass wire. The test piece was cut through the center of the penetration crater, Figure 1, making a cut surface approximately 51 mm × 148 mm. A fixture was constructed to clamp the plate on both sides of the cutting plane to prevent the EDM wire from moving off the cut plane. The 148 mm long cut took nearly 13 hours to complete. "Skim cut" settings, which are normally used for better precision and a finer surface finish, were used to minimize any recast layer and cutting-induced stresses. Under such conditions, EDM cutting has been demonstrated to not significantly affect residual stress measurement [24]. Contour method measurements on a weldment with very high stresses were validated independently [23], which also gives confidence that EDM cutting will not affect the residual stress measurements reported in this paper.

After cutting and unclamping, the contours of both cut surfaces were measured using a MS Impact II Coordinate Measuring Machine (CMM), which touches the surface with a small trigger probe to map the surface contour. A 1 mm diameter spherical ruby tip was used on the probe. The cut surfaces were measured on 0.5 mm spaced grids, giving about 29,000 points on each cut surface.

Figure 4 shows data points measured on one of the two halves after cutting. The peak-to-valley range in the contour is about 150 μm. The most striking feature in the contour

is the large bump centered about one crater diameter below the impact crater. The contour on the other half was very similar.

A test cut was made near the edge of the plate to validate the assumption of a planar cut. The free-surface condition in this area should result in stresses, and thus deformations, that are less than 10% of the values expected in the central region of the plate. The measured contour from this cut was less than 6 μm peak-to-valley. This is consistent with our expectations and thus validates our flat cut assumption.

The residual stresses were calculated from the measured surface contours using a static, elastic FE model and the commercial code ABAQUS. A 3-D model was constructed of one half of the plate, the condition after it had been cut in two, including the crater as a pre-existing feature. The mesh was graded with a minimum element size of about 1 mm, resulting in 116,980 linear shape–function (i.e., 8 node) brick elements and 375,408 degrees of freedom. The material behavior for HSLA-100 was modeled as isotropic elastic with the elastic modulus and Poisson's ratio shown in Table 3.

In order to smooth out noise in the measured surface data and to enable evaluation at arbitrary locations, the data were fitted to smoothing splines. A detailed description of this process is given elsewhere [23], including how to objectively choose the amount of smoothing and estimate the uncertainties in the calculated stresses. The spline fits to the measured contour data were evaluated at a grid corresponding to the FE nodes, averaged between the two sides, the signs reversed, and then applied as z-direction displacement boundary conditions on the cut surface in the model. Three additional displacement constraints were applied to prevent rigid body motions, and no other constrains or boundary

conditions are applied to the model. Figure 5 shows the deformed FE model, which as explained shows the opposite of the measured contour of Figure 4. The surface stresses were then obtained by evaluating the values of σ_z at the nodes of the surface elements and averaging among all elements sharing a given surface node.

Numerical Model

The predicted residual stresses from the dynamic impact were estimated from an explicit finite element calculation using LS-DYNA, which is a commercially available Lagrangian code [25]. An axisymmetric finite-element model was generated for the analysis of the plate and sphere using 4-node elements. The mesh for the ball consisted of 467 elements with an element size of approximately 0.2 mm. The mesh for the plate consisted of 22,500 elements, with a graded distribution. The smaller elements in the plate, which were nearest the point of impact, had a minimum element size of 0.4 mm.

Our calculations used the most elementary hydrodynamic material model available in LS-DYNA that utilizes both an Equation of State (EOS) and Failure. Both of the materials used the same elastic-plastic hydrodynamic material model (Mat 10) in LS-DYNA with a Grüneisen EOS. The implementation of this elementary hydrodynamic material model did not include a pressure cutoff, or temperature and rate sensitivity, but simply a tabulated form of the flow stress as a function of strain. Therefore, the flow stress for a given state of strain was determined computationally by interpolation within the tabulated values. The motivation for this was due in part to the availability of constitutive data for the materials of interest. However, as will be shown later, the results were surprising good.

The flow stress data for the HSLA material were determined from Instron testing performed at Los Alamos National Laboratory [26] and are presented Figure 6 for a strain-rate of 0.001/s at 49°C. An elastic-perfectly plastic data set was used for the spheres based on physical properties and ultimate strength published by Johnson [27]. Failure strains of 0.8 and 0.007 were respectively defined for the plate and sphere materials. However, the material model used for this simulation does not conserve mass or energy when an element is eroded at the specified failure strain. In addition, the tension spall option was activated for the tungsten carbide. The constitutive properties for both materials are provided in Table 3.

The LS-DYNA simulations presented here are not sophisticated and are recognized to have limitations with regard to variations in strain-rate, temperature, and failure. LS-DYNA has more advanced models such as Johnson-Cook. However, these models were not used due to the limited amount of constitutive data for the materials. Documented failure strains were unavailable and credible values of 0.8 and 0.007 were arbitrarily selected.

The time step for the analysis was 2 nsec. A sequence of six images, illustrating a section of the finite element mesh for the ball and plate, are shown Figure 7. The timeframe illustrated in this figure spans from 0 to 11 μsec, at which time the ball has been completely eroded and approximately 380 elements in plate have been eroded. The numerical calculation was continued to 52 ms to obtain ensure a reasonably steady stress state for the residual stress prediction.

Results

The numerical predictions for both crater width and depth are shown as a function of velocity in Figures 8 and 9, respectively. The relationship between the crater depth and the

impact velocity is shown to be much more linear in numerical predictions than indicated by the experimental data. The error in the values presented for the numerical predictions is on the order of the element size, since an entire element is eroded at once and the depth of penetration is based on the nodal position of the remaining elements. The resulting crater shape from this impact is examined further in Figure 10 with a comparison between the finite element model and the experimental data.

Figure 11A shows the map of residual stress (σ_z) measured by the contour method, and Figure 11B shows the prediction from the finite element model, where the hoop stress in the axisymmetric model corresponds with the measured σ_z. Good agreement between the model and the measurements is especially evident in the region of compressive stress centered about one crater diameter below the bottom of the crater. The size and shape of the compressive region is similar between the prediction and the measurement. The model predicted a peak compressive stress of 1100 MPa and the measurements gave a value of 1095 +/- 25 MPa. This agreement is excellent considering the highly nonlinear nature of the impact event, the large range of strain rates and the localized temperatures experienced during the impact. However, the model did not account for existing residual stresses in the plate before the impact event, which are expected to alter the predictions. Note that the peak σ_z compressive stress significantly exceeds the yield strength of about 720 MPa because the stress is highly triaxial in this region, thus the effective stress is significantly lower than maximum stress component. For the element with the peak hoop stress of -1100 MPa, the model predicted radial stress of -696 MPa and axial (y) stress of -896 MPa, which, combined with non-zero shear stresses, give an equivalent von Mises stress of only 500 MPa.

Individual residual-stress components exceeding the yield strength because of triaxiality have been observed routinely, usually in tensile stress regions of welds [* MERGEFORMAT 28].

The agreement between the prediction and the measurement is less evident in other regions of the stress map due to the initial residual stresses in the plate prior to the impact. The numerical model assumed an initial stress free condition. Examination of Figure 11A reveals a background residual stress distribution of compressive stress near the top and bottom surfaces of the plate and tensile in the center, typical of quenching stresses.

To evaluate the effect of initial residual stresses, a stress map was measured on a plate of HSLA-100 material that had not been impacted. Because it was the only piece available, a 60.75 mm thick plate was tested using the contour method. This plate underwent the same processing and was expected to have very similar initial residual stresses to the 51 mm thick plate used in the impact experiments. Figure 12 shows the measured stress map in the thicker plate, which shows the expected quenching distribution of residual stresses. Note, the stress map in Figure 12 does not show the same high tensile stresses at the $+x$ and $-x$ edges as Figure 11A because the specimen measured for Figure 12 was saw cut along those edges from a larger plate whereas the specimen used for Figure 11A had been flame cut. Flame cutting, not surprisingly, produced much higher stresses.

A subsequent coarse attempt to account for the initial residual stresses proved to be surprisingly effective at reconciling the model predictions with the measurements. The initial residual stresses were not introduced directly into the LS-DYNA simulation due to resource limitations. Subsequent work and enhanced calculations may consider this capability to

provide a more direct comparison between the experimental data and numerical predictions. Therefore, a correction was made to the measured stress map presented here by subtracting off the initial residual stresses. Such a subtraction implies the stress maps can be superimposed, which obviously over-simplifies the highly nonlinear process. Nonetheless, the resulting stress map shown in Figure 13A agrees remarkably well with the model prediction of Figure 13B, where Figure 13B is an exact duplication of Figure 11B.

The residual stress results also confirm that the spacing between impact tests was sufficient to avoid interaction between the tests. At one plate thickness (51 mm) away from one impact site, the distance between tests, the residual stresses are essentially unaffected by the penetration. Furthermore, the stresses are less affected on the side opposite the impact, which justifies the experimental choice to use both sides of the target.

Conclusions & Observations

The complex cross-sectional residual-stress map in a penetrated plate was measured using the contour method. The stress map probably could not have been measured with any other technique because of the size of the specimen [29]. For example, measuring a comparable stress map with neutron diffraction would not have been practical because of the 51 mm thickness of the plate.

The impact produced a region of compressive residual stress exceeding the material's yield strength, located about one crater diameter below the crater floor, which is balanced by a region of tensile stresses located farther from the crater. This stress state may be a concern for subsequent loading, particularly for the tensile region, which extends to the surface of the

part and thus provides an area for the initiation of a crack. This issue should be addressed in a subsequent study.

The diameter and depth of penetration resulting from a high velocity impact by a small diameter tungsten-carbide sphere have been shown and compared with numerical predictions. The experimental data indicate that the diameter of the resulting crater increases linearly as a function of impact velocity. However, the relationship between velocity and the depth of penetration appears to be nonlinear over the velocity ranges studied here, in qualitative agreement with experimental observations reported elsewhere by Forrestal and Piekutowski [20] and by Stilp and Hohler [21].   A detailed physical explanation of the nonlinear impact velocity/depth of penetration relationship is given in [20] based upon experimental observations of penetration behavior of spherical-nose steel projectiles for a range in impact velocities overlapping the work reported herein. As discussed in the Experiments Section above, Forrestal and Piekutowski [20] identified three response regions as striking velocities of the projectiles increased, using post-test radiographs of the targets. However, these response regions are not fully applicable for the brittle spherical projectiles impacted in the present study, notwithstanding the qualitative agreement in the general shape of the penetration depth vs. velocity curve.

The data presented here are insufficient to fully explain this observation. Studies discussed in the background above suggest that fragmentation behavior of spheres may vary with velocity. Grady's [10] experiments, which were conducted at velocities between 2.1-4.0 km/sec, suggest that the fragmentation cloud from higher velocity impacts is much more

dispersed with more radial separation at the front of the impact. Piekutowski [17] observed similar behavior for aluminum spheres traveling between 2-4.6 km/sec and reported a failure transition at velocities above 2.6 km/sec. These studies, in addition to phase change studies by Williams [11] and Hertel et al. [15], may provide valuable insight into the penetration behavior observed in Figure 9.

Overall, the explicit finite-element model gave excellent agreement with the residual stress measurements for the single case investigated, especially considering the elementary nature of the material model. Marginal agreement is shown for the crater geometry, and the simulations did not predict the non-linear relationship observed in experimental data between the depth of penetration and velocity. The model predictions may have been improved by including the initial residual stresses in the plate in the calculations. The agreement in this area may also have been affected by the spall or phase change phenomenon discussed above. A strain-rate dependent constitutive model may also be important, particularly in this type of calculation where the simulation spans from the high-velocity impact to the quasi-static state of equilibrium. Future work should include more realistic failure parameters based on physical data as well as more physically based strength, damage, and failure models.

Acknowledgement

References

[1] Cowles BA. High cycle fatigue in aircraft gas turbines: An industry perspective. Int J Fract 1996; 80(2-3): 147-163.

[2] Mall S, Hamrick JL, Nicholas T. High cycle fatigue behavior of Ti-6Al-4V with simulated foreign object damage. Mech Mater 2001; 33(11): 679-692.

[3] Thompson SR, Ruschau JJ, Nicholas T. Influence of residual stresses on high cycle fatigue strength of Ti-6Al-4V subjected to foreign object damage. Int J Fatigue 2001; 23(SS): S405-S412.

[4] Peters JO, Boyce BL, Chen X, McNaney JM, Hutchinson JW, Ritchie RO. On the application of Kitagawa-Takahashi diagram to foreign-object damage and high-cycle fatigue. Eng Fracture Mech 2002; 69 (13): 1425-1446.

[5] Chen X, Hutchinson JW. Particle impact on metal substrates with application to foreign object damage to aircraft engines. J. Mech Phys Solids 2002; 50 (12): 2669-2690.

[6] Lanciotti A, Ottaviano S. Some fracture mechanics properties in high-velocity impact-damaged aluminium plates: Fatigue Fract Engng Mater Struct 2001; 24(6): 419-427.

[7] Reimers W, Broda M, Brusch G, Dantz D, Liss KD, Pyzalla A, Schmackers T, Tschentscher T. Evaluation of residual stresses in the bulk of materials by high energy synchrotron diffraction: J Nondes Eval 1998; 17(3): 129-140.

[8] Webster PJ, Oosterkamp LD, Browne PA, Hughes DJ, Kang WP, Withers PJ, Vaughan GBM. Synchrotron X-ray residual strain scanning of a friction stir weld: J Strain Anal Engng Des 2001; 36(1): 61-70.

[9] Boyce BL, Chen X, Hutchinson JW, Ritchie RO. The residual stress state due to a spherical hard-body impact: Mech Mater 2001; 33(8): 441-454.

[10] Grady DE. "Impact failure and fragmentation properties of tungsten carbide", Int. J. Impact Engineering, 1999; 23(1): 307-317.

[11] Williams AE. "The effect of phase changes on target response", Int. J. Impact Engineering, Vol. 1995; 17: 937-947.

[12] Wang A, De Souza UJ and Rack HJ. "Impact deformation and damage of a high chromium white cast iron by spherical projectile at normal incidence:", Wear, 1991; 151: 157-173.

[13] Tanabe Y, Saitoh T, Akatsu T, and Sawaoka A. "Crater formation of carbon materials by impact of a high velocity sphere", Carbon, Bol. 33, 1995; 11: 1547-1552.

[14] Grady DE and Kipp ME. "Experimental and computational Simulation of the High Velocity Impact of Copper Spheres on Steel Plates", Int. J. Impact Engineering, 1994; 15: 645-660.

[15] Hertel ES Jr., McIntosh RL, and Patterson BC. "A comparison of phase change phenomena in cth with experimental data", Int. J. Impact Engineering, 1995; 17: 399-408.

[16] Orphal DL. "Highly oblique impact and penetration of thin targets by steel spheres", Int. J. Impact Engineering, 1999; 23(1): 687-698.

[17] Piekutowski AJ. "Fragmentation of a sphere initiated by hypervelocity impact with a thin sheet", Int. J. Impact Engineering, 1995; 17: 627-638.

[18] Hayhurst CJ, Ranson HJ, Gardner DJ, and Birnbaum NK. "Modelling of microparticle hypervelocity oblique impacts on thick targets", Int. J. Impact Engineering, 1995; 17: 375-386.

[19] Prime MB. Cross-sectional mapping of residual stresses by measuring the surface contour after a cut. J. Engng. Mater. Tech. 2001; 123(2): 162–168.

[20] Forrestal MJ, Piekutowski AJ. Penetration experiments with 6061-t6511 aluminum targets and spherical-nose steel projectiles at striking velocities between 0.5 and 3.0 km/s. Int J Impact Eng 2000;24:57-67.

[21] Stilp AJ, Hohler V. Long-rod penetration mechanics. In: J.A. Zukas, editor. High velocity impact dynamics. New York, NY: Wiley, 1990 [Chapter 5].

[22] Bueckner HF. The propagation of cracks and the energy of elastic deformation. Trans Amer Soc Mech Engineers 1958; (80): 1225–1230.

[23] Prime MB, Sebring RJ, Edwards, JM, Hughes JD, Webster PJ. Laser surface-contouring and spline data-smoothing for residual stress measurement. Exptl Mech; submitted 2003.

[24]Cheng W, Finnie I, Gremaud M, Prime MB. Measurement of near-surface residual-stresses using electric-discharge wire machining. J. Engng Mater Tech 1994; 116(1): 1-7.

[25] LS-DYNA. Version 950, Users Manual, Livermore Software Technology Corporation, June 1997.

[26] Chen SR. private communication.

[27] Johnson AE Jr.. National Advisory Committee for Aeronautics, Technical Note 3309, (1954).

[28] Webster GA, Ezeilo AN. Residual stress distributions and their influence on fatigue lifetimes. I. J. Fracture 2001; 23(SS): S375-S383.

[29] Withers PJ, Bhadeshia HKDH. Overview : Residual stress part 1 : Measurement techniques. Mat Sci & Tech 2001; 17(4): 355-365.

Table 1. Chemical composition of HSLA-100 steel plate in wt-%.

Fe	C	Mn	P	S	Cu	Si	Ni	Cr	Mo	V	Ti	Al
92.6	0.06	0.85	0.005	0.002	1.56	0.26	3.45	0.56	0.58	0.003	0.001	0.025

Table 2. Impact velocity and resulting crater diameter, depth, and volume from impact
experiments.

Shot #	Velocity (km/sec)	Diameter (mm)	Depth (mm)	Volume (ml)
1	0.83	6.35	4.57	0.11
2	0.97	6.60	5.59	0.17
3	0.98	6.53	5.46	0.16
4	1.27	7.49	7.09	0.24
5	1.28	7.29	6.86	0.26
6	1.50	8.00	8.51	0.35
7	1.81	8.92	8.79	0.5
8	1.91	9.27	8.53	0.5
9	2.15	9.91	8.41	0.73
10*	**2.22**	**10.03**	**8.64**	**0.66**
11	2.46	10.87	9.50	0.93
12	2.55	11.43	9.60	1

* Experiment selected for residual stress comparison

Table 3. Constitutive properties for the HSLA-100 plate and Tungsten-Carbide spheres.

Material	Description	Value	Units
HSLA Plate	Density	7.842	g/cm^3
	Shear Modulus	76.3	GPa
	Elastic Moduls	197.0	GPa
	Yield Stress	730.0	MPa
	Poisson's Ratio	.29	
	Failure Strain	0.8	
	Grüneisen Gamma	2.17	
	Intercept of Us-Up Curve	3.92x10^5	
	S1	1.586	
Tungsten-Carbide Spheres	Density	14.9	g/cm^3
	Shear Modulus	251.0	GPa
	Elastic Moduls	683.0	GPa
	Yield Stress	3.63	GPa
	Failure Strain	0.015	
	Grüneisen Gamma	1.50	
	Intercept of Us-Up Curve	5.19x10^5	
	S1	1.16	
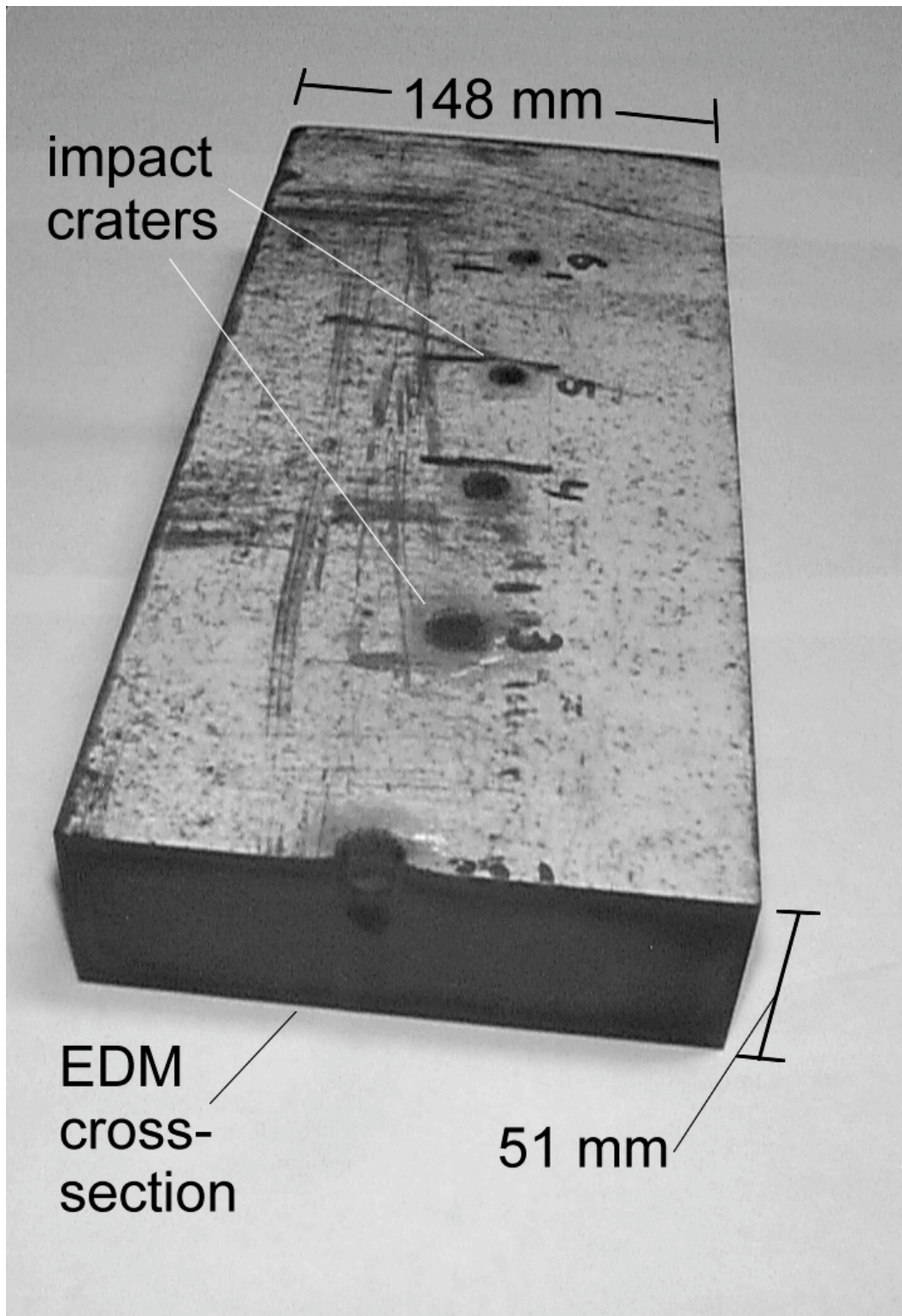
Figure 1. Plate used in impact experiments, showing multiple craters and EDM cut used to measure residual stress.
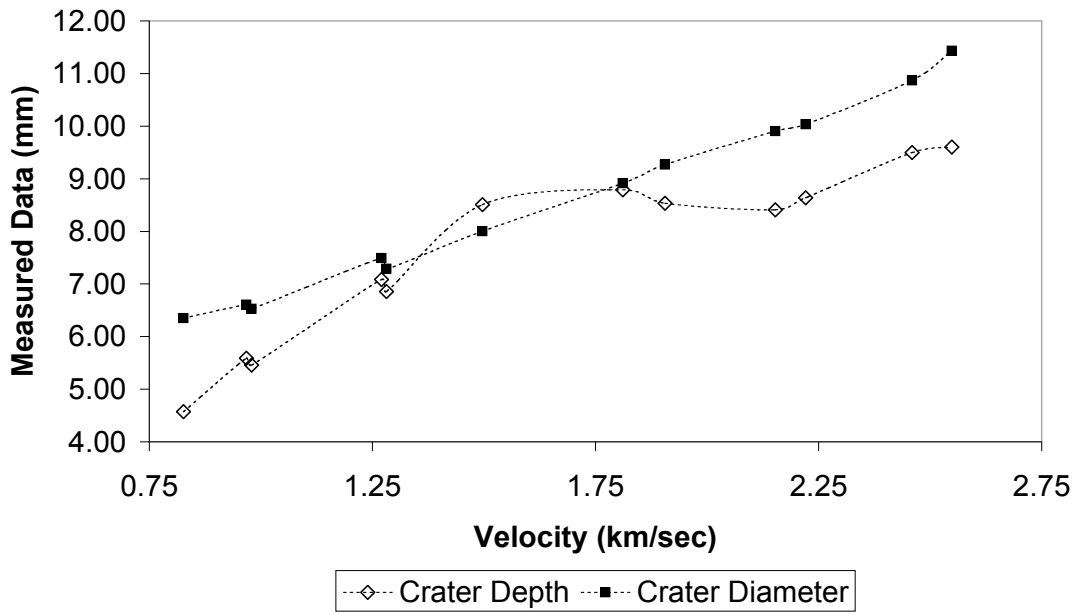
Figure 2. Crater depth and diameter from impact experiments.
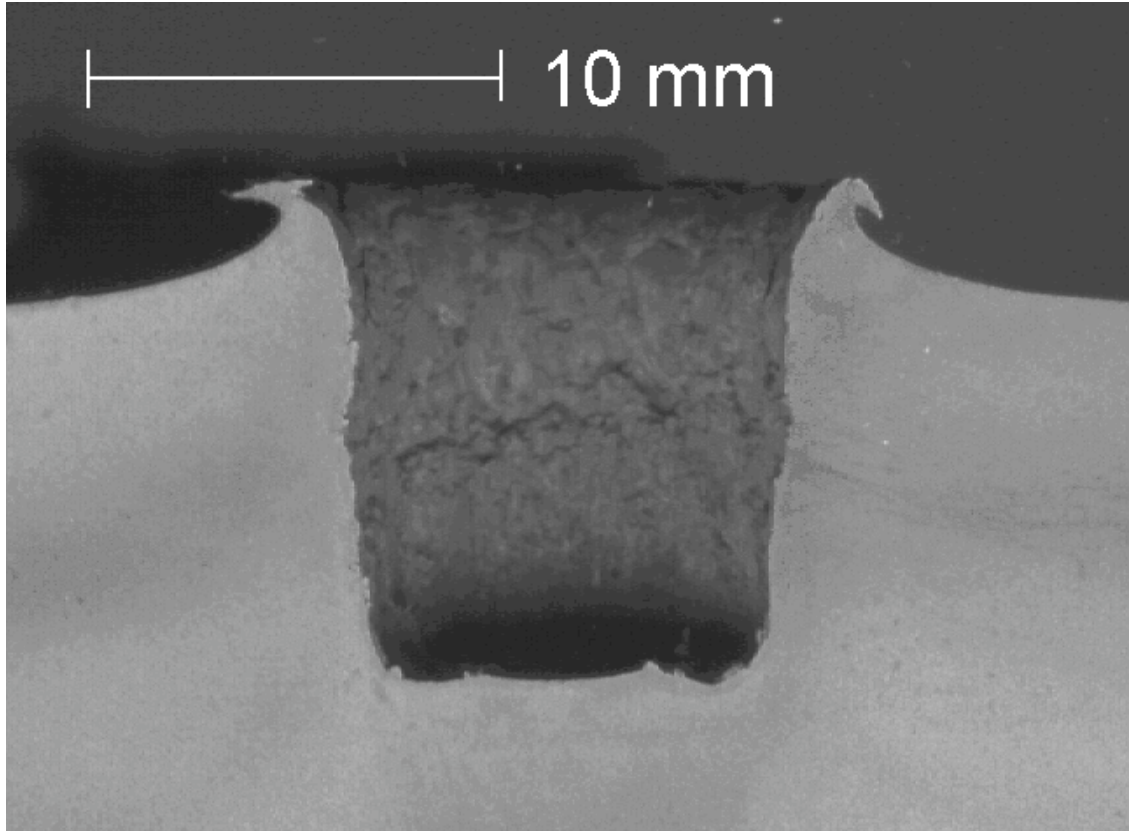
Figure 3. Cross-section of crater from 2.2 km/sec ball impact.
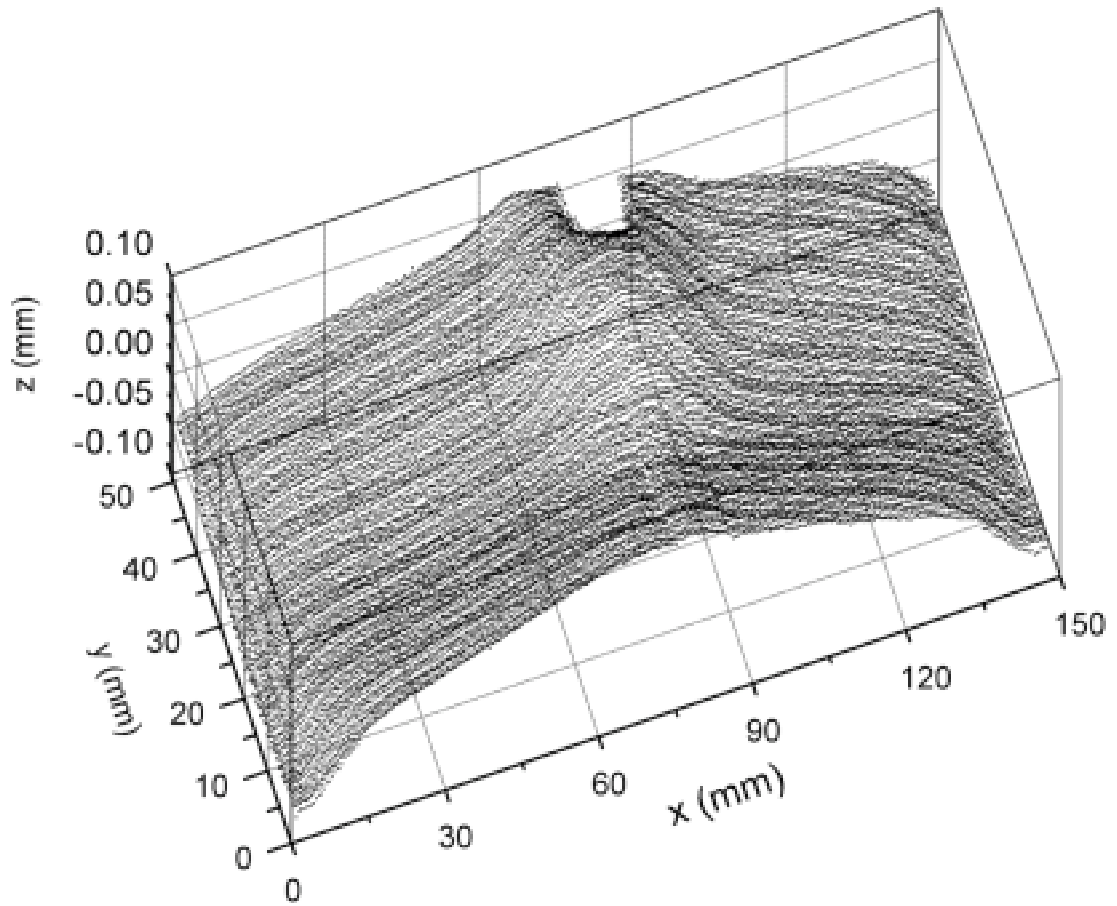
Figure 4. Surface contour measured by the Coordinate Measuring Machine after cutting
specimen.
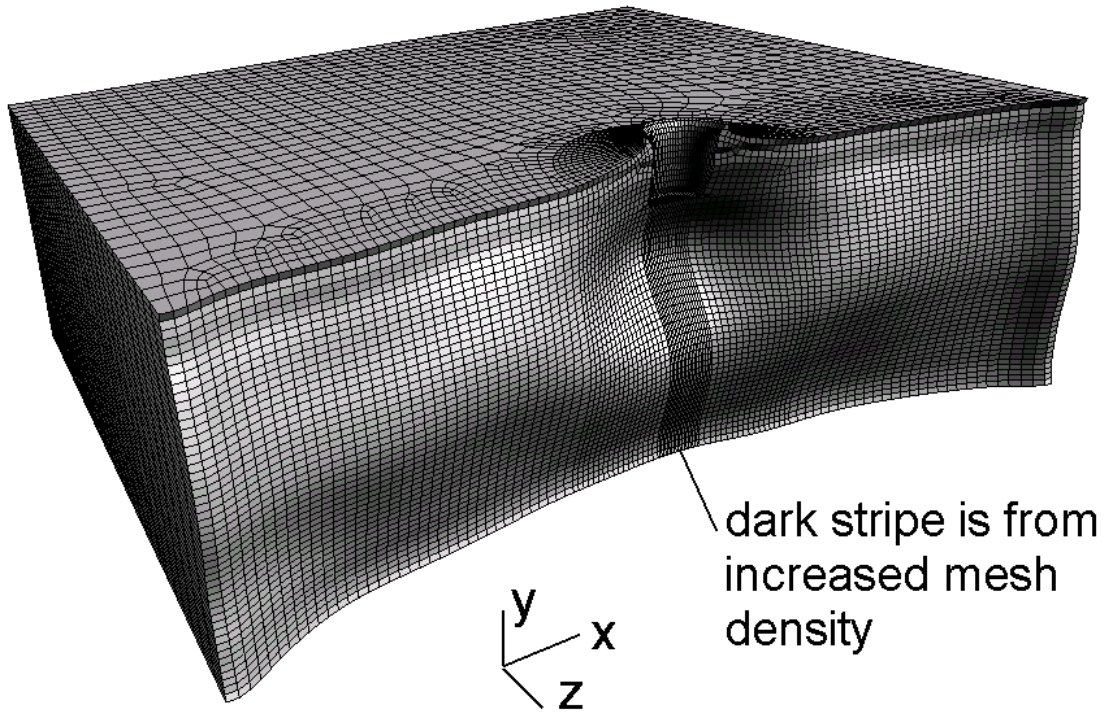
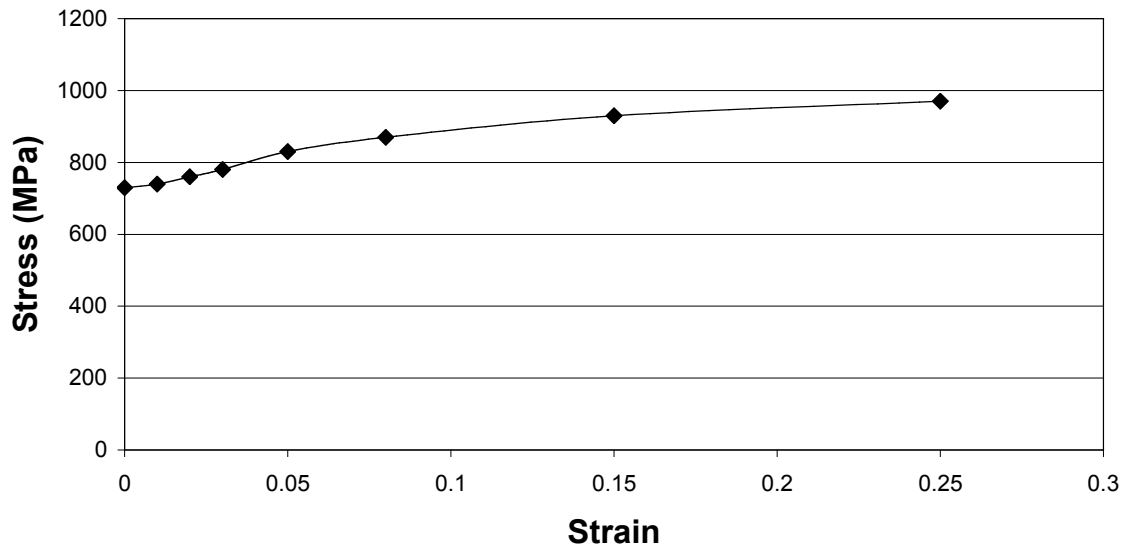Figure 5. Finite element model used to calculate residual stresses from contour method measurement. Shown after applying displacement boundary condition to cut surface.

Figure 6. Flow Stress for HSLA-100 plate for a strain-rate of 0.001/s at 49°C [26].

0.0 µs   2.0 µs   4.0 µs

6.0 µs   8.0 µs   11.0 µs
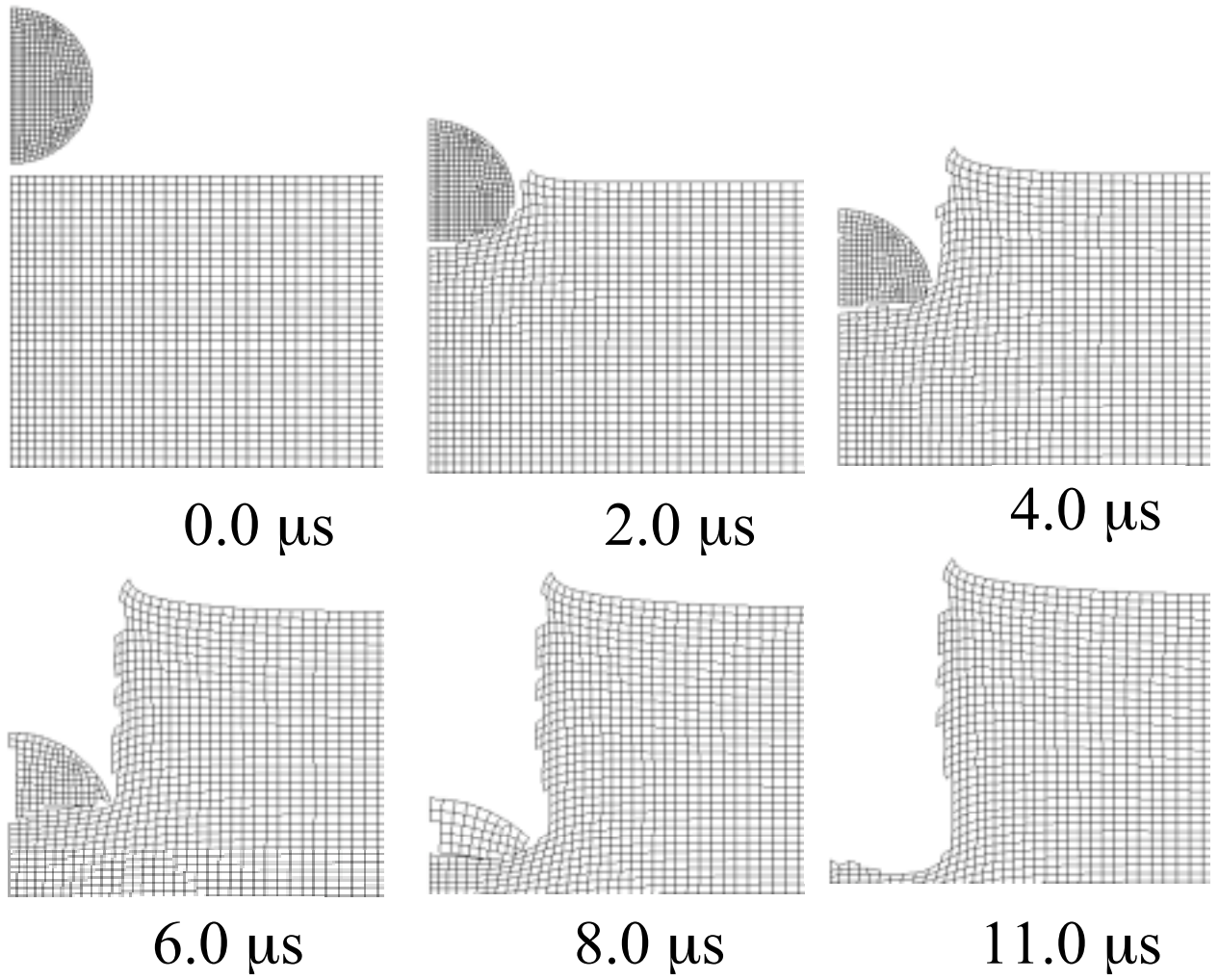
Figure 7. Section of the Finite Element Mesh Illustrating Element Erosion from

0-11 µsec
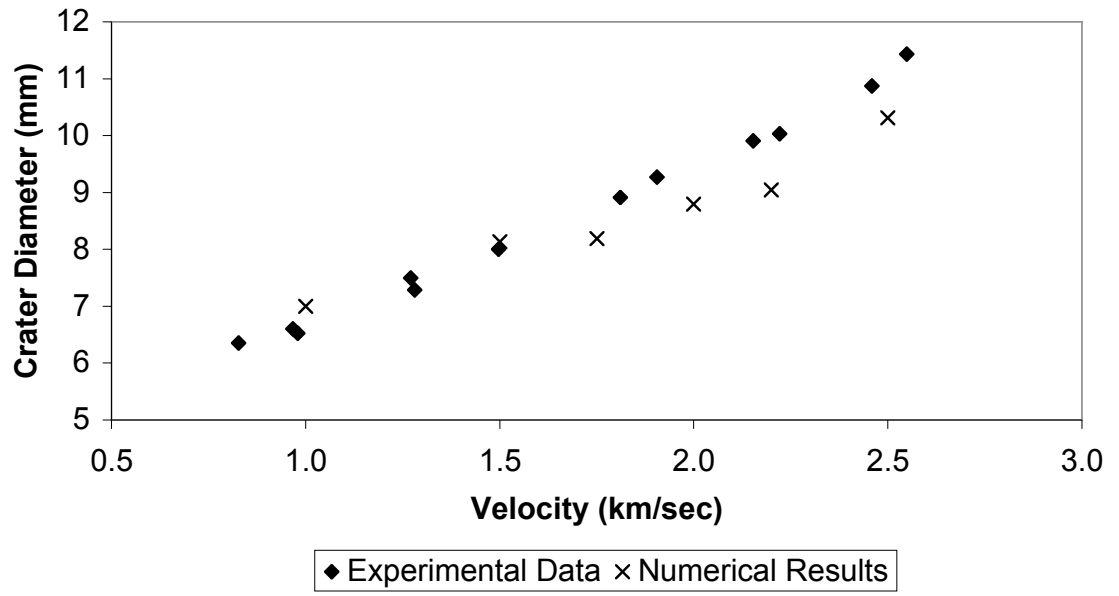
Figure 8. Crater Diameter from experimental data and numerical model.
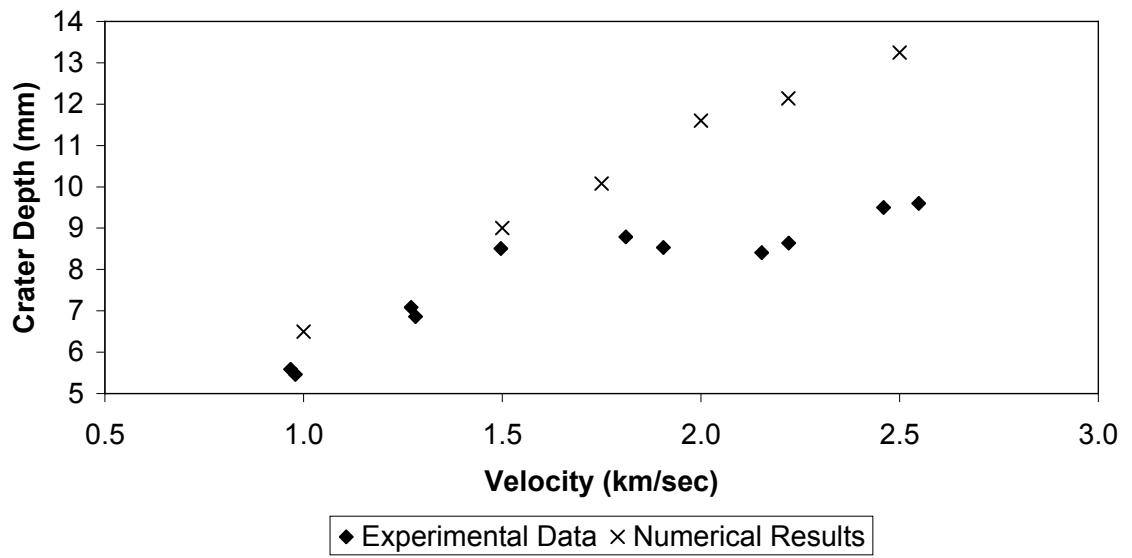
Figure 9. Crater depth from experimental data and numerical model.
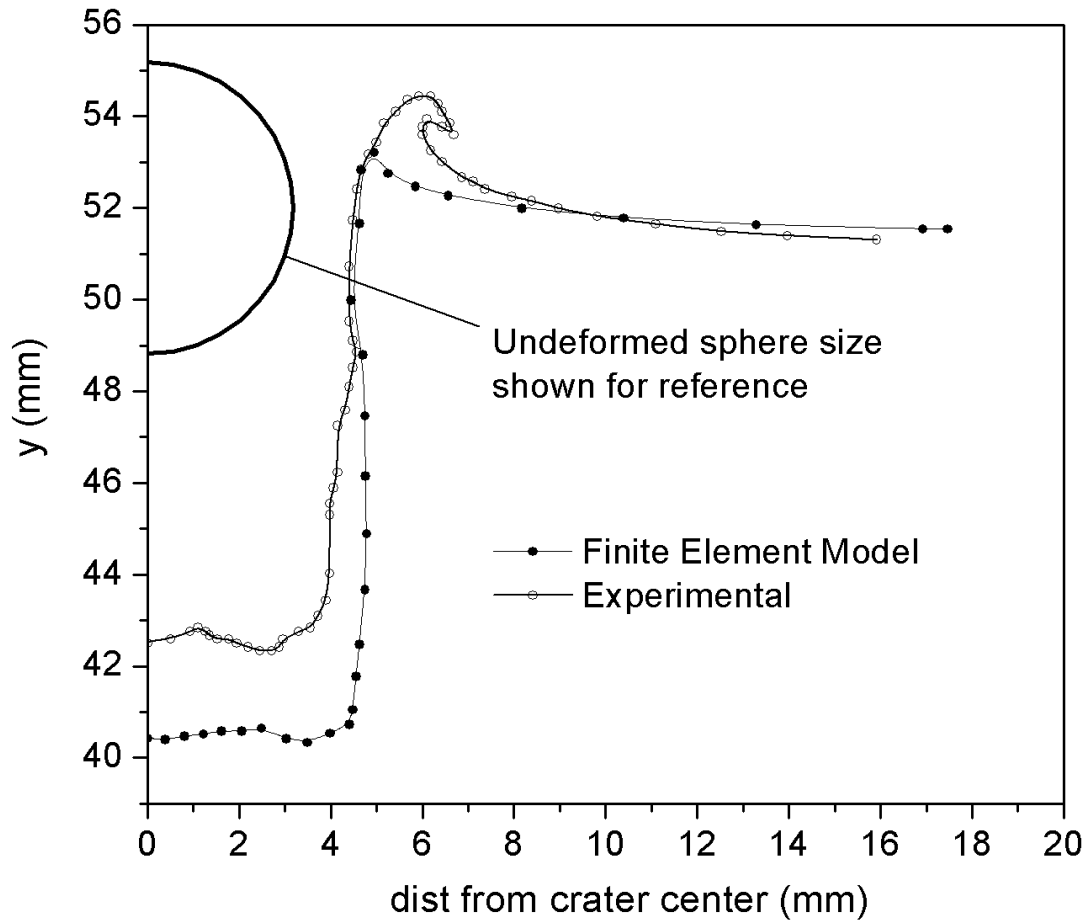
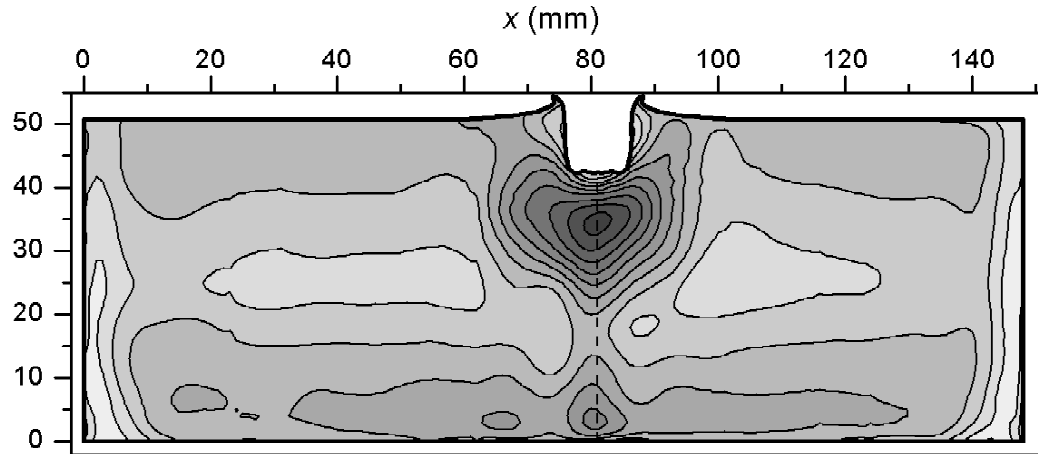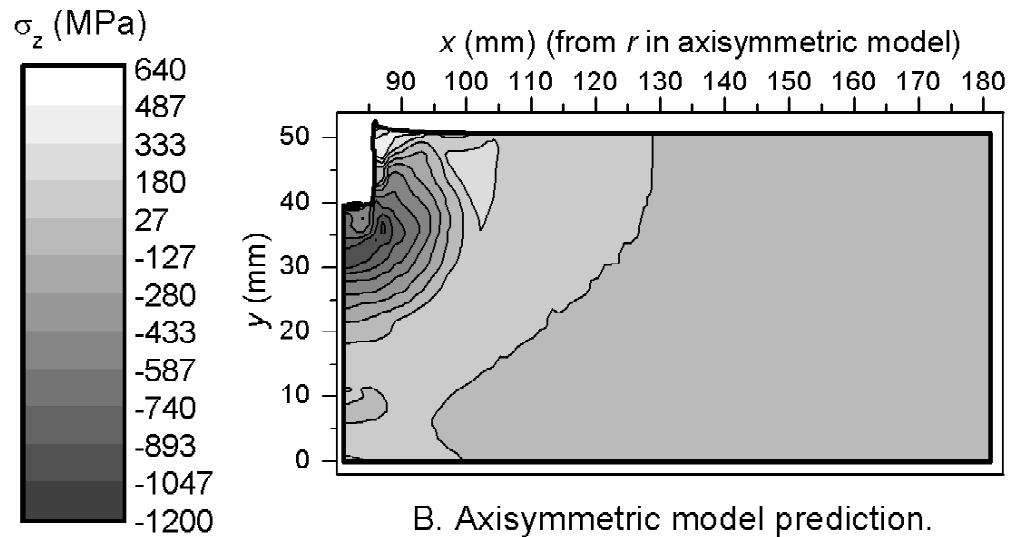Figure 10. Measured and calculated crater shape from 2.2 km/sec ball impact.

x (mm)

A. Measured residual stress map.

σ_z (MPa)

640
487
333
180
27
-127
-280
-433
-587
-740
-893
-1047
-1200

x (mm) (from r in axisymmetric model)

y (mm)

B. Axisymmetric model prediction.

Figure 11. Residual stresses in HSLA-100 plate after penetration by tungsten carbide sphere. A. Measured by contour method. B. Hoop stress prediction from lagrangian, explicit, axisymmetric model, shown on half of cross-section.
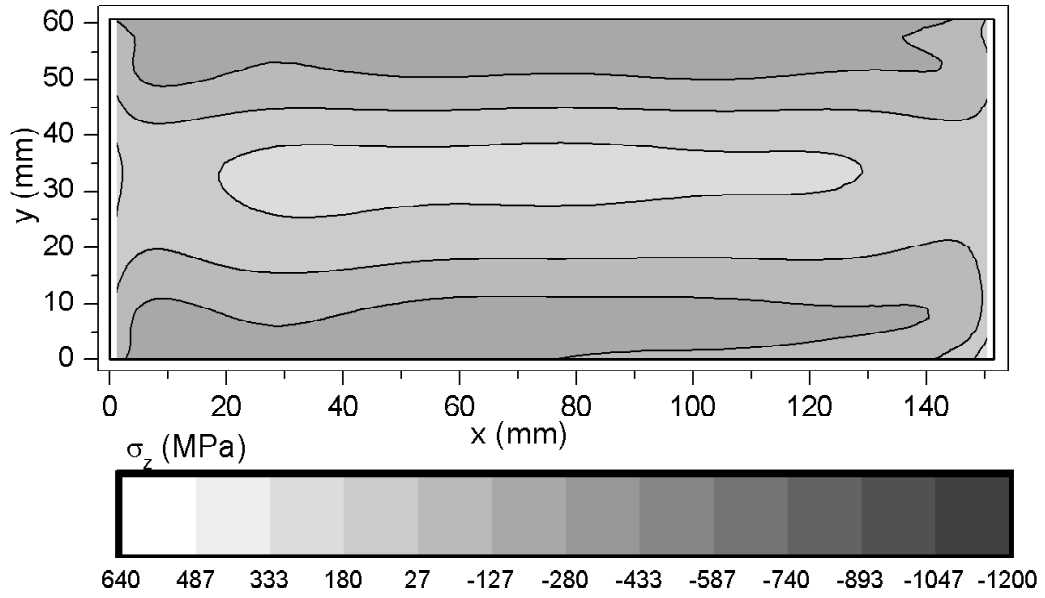
Figure 12. Residual stress map measured in as-received plate by contour method, shows original quenching stresses. Scale is the same as shown in Figure 11.
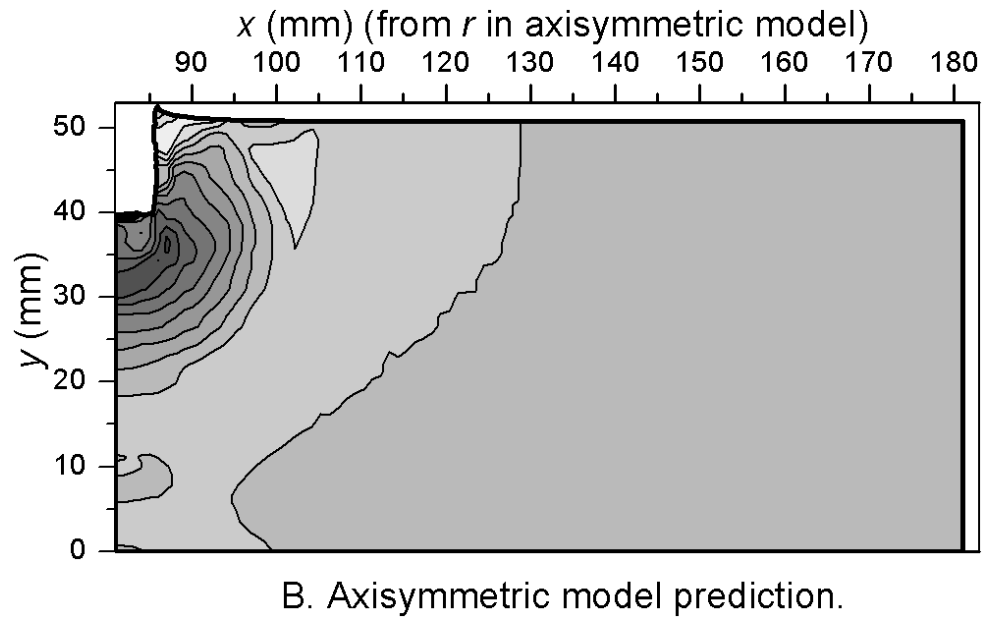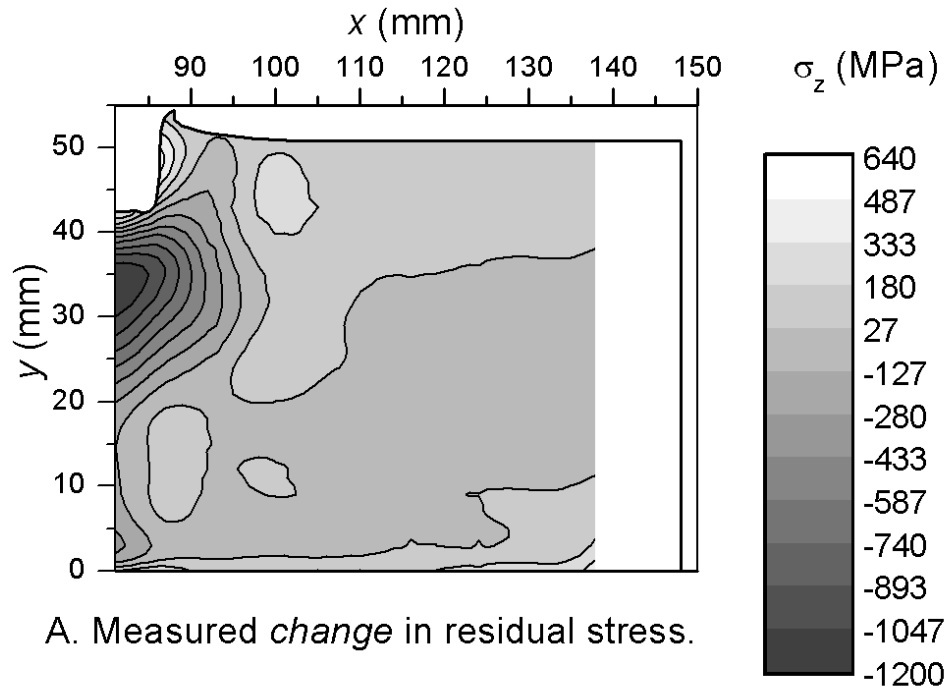
Figure 13. Residual stresses corrected for initial stresses. A. Measured *change* in residual stresses, i.e., Figure 11A minus Figure 12. B. Axisymmetric model prediction duplicated from Figure 11B, shown here for comparison.